INTERNATIONAL JOURNAL OF OPTIMIZATION IN CIVIL ENGINEERING
Int. J. Optim. Civil Eng., 2025; 15(3): 335-358

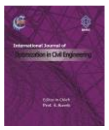

ON THE ROLE OF INPUT SIGNALS IN STRUCTURAL DESIGN BY SOUND ENERGY OPTIMIZER: A CASE STUDY

M. Shahrouzi[*, †] and A.M. Taghavi
Civil Engineering Department, Faculty of Engineering, Kharazmi University, Tehran, Iran

ABSTRACT

Sound Energy Optimizer (SEO) is a recent metaheuristic algorithm inspired by the propagation and reception of sound waves in physical environments. While conventional metaheuristics that rely on random number generators with certain distributions, SEO can utilize various real-world or simulated sound signals as the source of stochasticity to guide its search process. Concerning structural design by SEO, the effect of natural sound signals is compared with the artificial signals generated from uniform or normal distributions. In this regard, a 244-bar power transmission tower and a 1016-bar double-layer grid are simultaneously optimized with continuous geometry as well as discrete sizing variables to evaluate the impact of input signals on convergence behavior, solution quality and robustness of the algorithm. A sensitivity analysis is conducted to calibrate key control parameters of SEO. The results declare that the nature of the input sound signal can significantly affect the algorithm's exploration-exploitation balance. In this study, the "Knocking sound" signal yields the best performance, while the synthetic random signals revealed less stable optimization trajectories.

Keywords: sound energy optimizer, signal processing, physics-based meta-heuristic algorithm, random numbers, structural design.

Received: 16 July 2025; Accepted: 4 September 2025

1. INTRODUCTION

Structural engineering optimization problems with discrete variables pose significant challenges compared with their continuous counterparts, primarily due to the discontinuous nature of the

[*]Corresponding author: Civil Engineering Department, Faculty of Engineering, Kharazmi University, Tehran & Karaj, Iran
[†]E-mail address: shahruzi@khu.ac.ir (M. Shahrouzi)

search space as well as its narrow feasible region. The inability to use gradient-based methods, the non-smoothness of the objective function, and the combinatorial complexity arising from the large number of possible combinations in selecting standard cross-sections are among the key factors that make solving such problems difficult. Moreover, practical design constraints and the necessity to comply with construction standards when restrict the design variables to a discrete set of allowable values, results in a rugged search space riddled with numerous local optima.

Over the recent decays, numerous metaheuristic algorithms have been developed to tackle engineering design problems. Flower Pollination Algorithm [1], Vibrating Particles System [2], Jaya Algorithm [3], Dolphine Echolocation Algorithm [4], Opposition-Switching Search [5,6], Water Evaporation Optimization [7], Coyote Optimization Algorithm [8], Plasma Generation Optimization [9], Marine Predator Algorithm [10], Escaping Bird Search [11], Fire Hawk Optimizer [12], Hippopotamus optimization algorithm [13] and Osprey Optimization Algorithm [14] can be mentioned among many others.

Sound Energy Optimizer (SEO) [15] is one a most recent algorithm in the category of physics-based metaheuristics, already employed to global and structural optimization. It is primarily inspired by the propagation and reception of sound waves in physical media, modeling the optimization process through simulating the behavior of sound energy diffusion in a virtual space. The sound signals can be sampled over time using digital microphones, converting them into discrete-time signals and storing them as numeric data. The result is used as input data within the computational framework of SEO, enabling an intelligent search process throughout the solution space based on a specific mathematical model. This approach facilitates the integration of real-world environmental information into the optimization process and, by leveraging the inherent characteristics of wave propagation, assists in discovering optimal solutions for engineering problems.

Some existing algorithms in the research literature are indirectly associated with acoustic behaviors and have occasionally been informally referred to as "sound-based algorithms" or "inspired by vocalization". For instance, the Harmony Search (HS) algorithm [16] is inspired by the musical improvisation process, where each candidate solution is treated as a musical note within a harmonic piece, and a "harmony memory" is employed to store and improve high-quality solutions. On the other hand, the Bat Algorithm (BA) [17,18] is based on the echolocation (biological sonar) behavior of bats in detecting the prey, utilizing acoustic parameters such as frequency, loudness, and pulse emission rate. However none of them directly leverages acoustic sound signals in their search, except the recently introduced Sound Energy Optimizer. SEO establishes a novel foundation for direct incorporation of physical signals and sound related phenomena to metaheuristic approaches.

Metaheuristic algorithms, generally utilize random numbers in some specific statistical distributions rather than using natural signals [15] or chaotic patterns [19–21]. In this study, the normal distribution is adjusted with zero mean and unit variance such that the generated values fall within the interval $[-1, +1]$, while the uniform distribution is defined in the standard interval $[0, 1]$ and can be linearly transformed into the interval $[-1, +1]$ through a simple linear mapping. These random numbers serve as primary components for generating synthetic audio signals. By producing a large volume of random samples from such distributions, it becomes possible to simulate input signals with diverse statistical characteristics. This approach enables a systematic investigation on the impact of different random distributions in comparison to patterns of audio signals on the performance of SEO.

The present study is structured within five sections: In Section 2, the conceptual framework

and theoretical foundations of the sound energy optimizer (SEO) are briefed, detailing its implementation steps. Section 3 analyzes the differences between sound signals generated using normal and uniform distributions, discussing their parameters in comparison with natural sound signals. In Section 4, after conducting a sensitivity analysis to tune the effective parameters of a virtual sound controller device, performance of SEO is studied comparing input signals based on different distributions. It is further evaluated by solution of two large-scale structural design problems; including both geometry and sizing optimization. Finally, Section 5 is dedicated to summarizing the key findings, interpreting the results, and providing recommendations for future developments.

2. ALGORITHMIC IMPLEMENTATION OF THE SOUND ENERGY OPTIMIZATION

As outlined in the preceding section, SEO initiates with an input sound signal, that is first digitized and subsequently normalized to ensure compatibility with the computational framework. The normalized signal serves as the foundational excitation source within the virtual simulation environment. The algorithm of SEO is then executed through the following systematic steps:

2.1 Step 1: Initialization of Algorithmic Parameters

Set the control parameters of the algorithm, including the number of particles N, the maximum number of iterations (MI) or function evaluations (NFE_{max}), and the key parameters of the Virtual Sound Controller (VSC). VSC is a core component of the SEO framework, designated to emulate the behavior of a physical sound amplifier in the time-domain. It modulates the energy and waveform characteristics of the input signal through a set of tunable virtual parameters, analogous to control knobs on an audio device. VSC governs two principal operators: sound energy decay (SED) and probabilistic steps, which collectively simulate the attenuation of sound energy over time and introduce stochastic exploration into the search process, respectively. Operation and Exposition of the VSC architecture are detailed in [15].

For the optimization process, N particles are initialized by randomly distributing them across the feasible search space within the lower and upper bounds of the design variables. Each particle represents a candidate solution (design vector) on the objective function landscape. The current iteration counter CI is initialized to 1.

2.2 Step 2: Signal Injection into the Virtual Environment

The preprocessed (digitized and normalized) sound signal is introduced into the virtual environment. During this phase, the energy packets that correspond to zero amplitude signal samples are instantaneously dissipated, while non-zero energy components persist and contribute to dynamic evolution of the system.

2.3 Step 3: Evaluation and Identification of the Sensitive Particle

The objective (cost) function value (interpreted as potential energy) is computed for each particle in the population. The particle exhibiting the minimum objective value is distinguished as the Sensitive Particle (SP), representing the current best solution.

2.4 Step 4: Iterative Search Process

The main optimization loop is executed until one of the predefined termination criteria is satisfied. The loop proceeds as follows:

• Increment the iteration counter CI from 2 to MI , and update the Sound Life Time Factor (SLTF) according to Eq. (1):

$$SLTF = SEI \times Env(CI) \tag{1}$$

where CI and MI denote the current iteration and maximum iteration, respectively. SEI, or Sound Energy Intensity, acts as a scaling multiplicative factor for the normal envelope function, denoted by Env in Eq. (2). The parameters of Env (i.e., a, b, and c), are set to generate the desired pattern of sound energy decay.

$$Env(CI) = \left[1 - \left(\frac{CI - c \times MI}{MI - c \times MI} \right)^{b} \right]^{a} \tag{2}$$

• For each iteration, perform NPS (number of probabilistic steps) sub-iterations:

◦ Create a duplicate of the current SP position.
◦ Select a sound energy packet (SEP) to influence the SP.
◦ Update the selected SEP using the SLTF and the stray noise (SN) as per Eq. (3):

$$SEP = SLTF \times SN \tag{3}$$

◦ Generate a probabilistic transfer step (PTS) using Eq. (4):

$$PTS(j) = SEP \times SP(j) \tag{4}$$

◦ Compute the position of the new candidate sensitive particle (NCSP) via Eq. (5):

$$NCSP(j) = SP(j) + PTS(j) \tag{5}$$

◦ Evaluate the potential energy for the NCSP.
◦ If the potential energy of the NCSP is lower than that of the current SP, update the SP position to that of the NCSP.

• Termination Check: If $CI < MI$ or the total number of function evaluations (NFE) has not exceeded the maximum allowable limit $NFE < NFE_{max}$, increase CI and repeat the loop. Otherwise, proceed to Step 5.

2.5 Step 5: Output of the Optimal Solution

Upon satisfaction of the termination condition (by reaching either MI or NFE_{max}) the updated position of the sensitive particle is reported as the optimal solution.

The termination mechanism prevents excessive resource consumption while allowing sufficient exploration of the search space.

3. SOUND SAMPLES OR RANDOM NUMBERS

In the present case study, two synthetic signals are considered with uniform and normal distributions, as well as two natural signals; i.e. a Wolf sound and a Door knocking sound. Figure 1 compares distribution of these signals regarding their probability density.

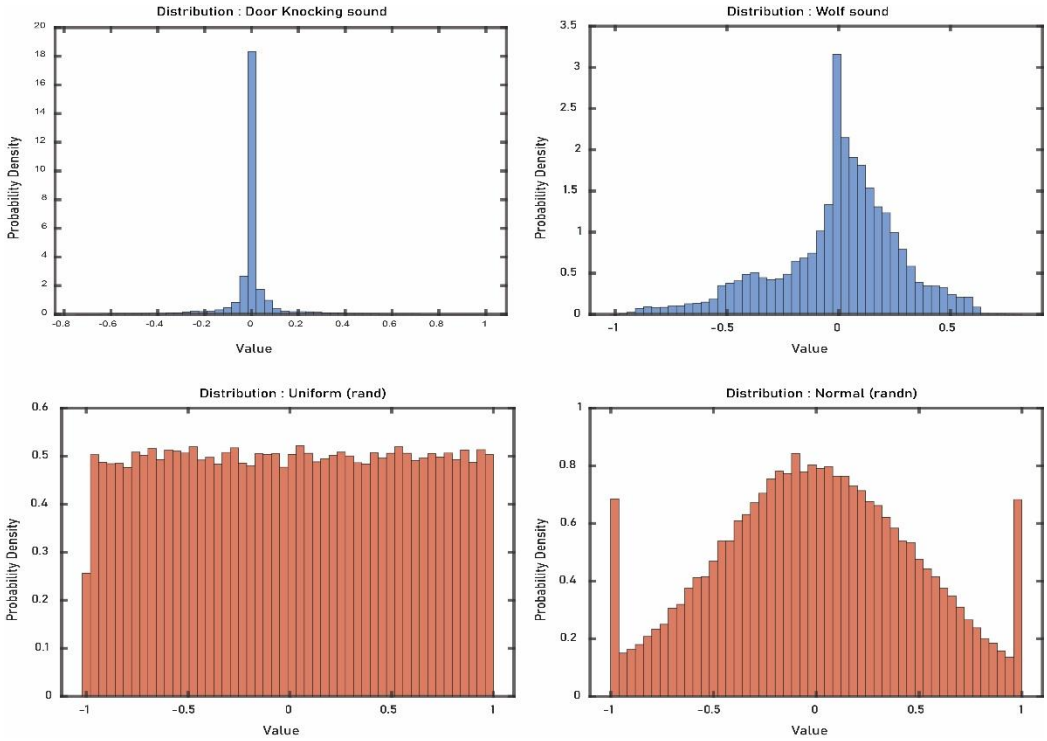

Figure 1: Probability density of the treated artificial and natural sound signals

Such distributions are transferred to the exploration and exploitation mechanisms in the algorithm. While the "Uniform" distribution exhibits a flat density [−1,1], promoting maximal exploration through unbiased sampling, bell-shaped curve of the "Normal" distribution supports a balanced trade-off between exploration and exploitation by concentrating search efforts around the mean and allowing occasional long-range jumps. Notably, natural sounds such as "Door knocking sound" and "Wolf sound" display non-uniform, structured distributions: the former is sharply peaked about zero, indicating a strong bias toward exploitation in localized regions, where the latter shows a broader, asymmetric spread, suggesting moderate exploration with directional preference, akin to modulated stochastic search behavior. These characteristics demonstrate that real-world audio signals inherently embody dynamic statistical properties similar to those intentionally engineered in metaheuristic processes. Consequently, natural sound distributions can serve not only as biologically plausible models of stochasticity but also as effective sources of adaptive randomness, offering a novel pathway to balance exploration and exploitation in optimization algorithms by leveraging the intrinsic variability and temporal structure of auditory phenomena.

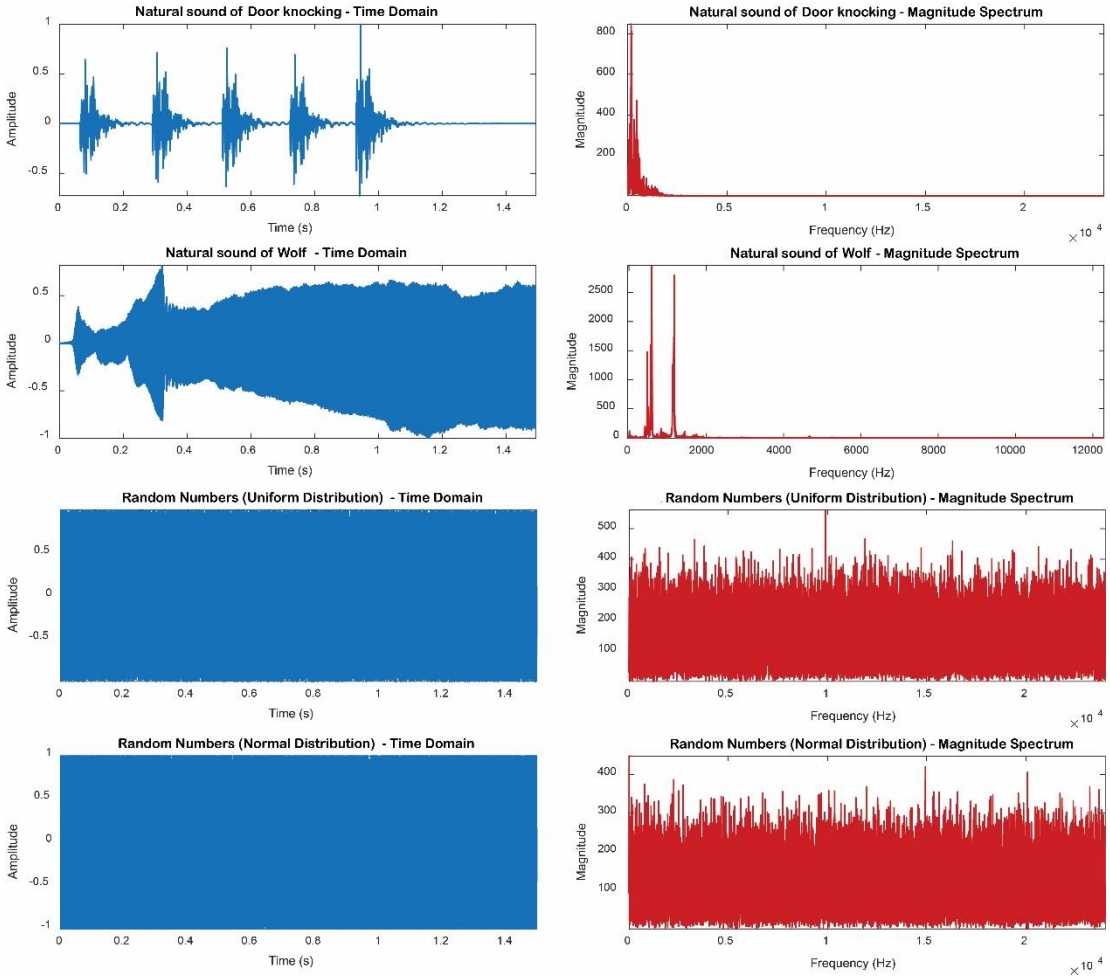

Figure 2: Time domain plots and Magnitude spectra for artificial and natural sound signals

The sound signals are also converted from the time domain to the frequency domain using the Fast Fourier Transform (FFT); allowing a detailed examination of their spectral characteristics. The extracted frequency-domain features, namely maximum magnitude (Max. Mag.), dominant frequency (Dom. Freq.), mean magnitude (Mean Mag.), energy, entropy, spectral centroid, and bandwidth, are summarized in Table 1. The time-domain waveforms (amplitude versus time) and their corresponding frequency-domain spectra (magnitude versus frequency) are shown in Figure 2, offering a comprehensive visualization of both temporal and spectral attributes of the signals.

Door knocking sound exhibits a relatively low max. magnitude (848.31) and dominant frequency (164.18 Hz), along with a low spectral centroid (257.15 Hz) and narrow bandwidth (173.77 Hz). By these characteristics it indicates energy concentration in the lower frequency range and a short, impulsive spectral profile. This corresponds to a transient, sparse signal with limited frequency spread; favoring exploitation due to its focus on a narrow region of the search space. In contrast, the sound of Wolf, shows a significantly higher max. magnitude (5792.65) and dominant frequency (584.35 Hz), with a higher centroid (738.32 Hz) and broader bandwidth (273.51 Hz), reflecting a richer, more sustained spectral structure. The matter offers a balanced but slightly exploration-biased behavior, as it covers a wider frequency band while maintaining energy concentration around dominant components.

On the other hand, both random signals display extreme spectral characteristics. The uniform random signal has a very high dominant frequency (9912.55 Hz), an extremely high spectral centroid (12023.77 Hz), and the largest bandwidth (6925.22 Hz), indicating widespread energy distribution across the frequency spectrum. This aligns with a pure exploration strategy, where the signal excites a broad range of frequencies, mimicking an algorithm's global search behavior. Similarly, the normal random signal also exhibits a high centroid (12050.81 Hz) and bandwidth (6957.95 Hz), despite a low dominant frequency (8.04 Hz), which may result from phase randomness rather than energy concentration. Its high entropy (10.0660) and energy values confirm a complex, unpredictable spectral structure, typical of stochastic processes used to maintain diversity in metaheuristic search.

Table 1: Features of four natural and artificial sound signals

Input Signal	Type	Centroid	Dominiat Frequency	Max. Magnitude	Mean Magnitude	Energy	Entropy	Band width
Door knocking sound	Natural	257.151	164.182	848.313	3.925	28097884.935	5.704	173.773
Wolf sound	Natural	738.318	584.352	5792.649	9.029	349044211.088	4.594	273.509
Random: Uniform	Artificial	12023.772	9912.548	561.510	137.054	855714143.011	10.065	6925.220
Random: Normal	Artificial	12050.809	8.041	447.750	113.920	590752002.295	10.066	6957.954

Notably, both random signals demonstrate significantly higher energy and spectral entropy with respect to the natural sounds, reflecting their sustained and irregular amplitude fluctuations over time. High entropy indicates greater spectral disorder, which is desirable in exploration phases to avoid premature convergence. In contrast, the lower entropy of the Door knocking and Wolf sounds reflects more structured, predictable patterns, suitable for fine-tuning solutions in exploitation phases.

To practically evaluate the impact of these acoustic signals on the optimization of real-world

structural problems, two complex, high-dimensional case studies will be solved in the following section by SEO under the influence of treated distinct input sound signals. It should be noted that, in addition to the inherent characteristics of each sound signal, SEO itself incorporates a unique decaying operator specifically designed to modulate exploration and exploitation. Such an operator is consistently applied to each sound signal, thereby ensuring a fair and balanced assessment of the individual effects of each acoustic input on the optimization performance.

4. OPTIMIZATION OF STRUCTURAL PROBLEMS

In this section, following the presentation of a general framework for formulating structural optimization problems, two numerical examples are presented in the fields of structural geometry and size optimization. Prior to performing the design, a sensitivity analysis is conducted on the key parameters of the SEO algorithm. Accordingly, the objective (cost) function is defined as [22]:

$$W\left(A,x\right)=\sum_{i=1}^{m}\rho A_i L_i=\sum_{i=1}^{m}\rho A_i\left[\sum_{j=1}^{3}\left(x_{ij}^{a}-x_{ij}^{b}\right)^2\right]^{\frac{1}{2}} \tag{6}$$

where

$$g_k\left(A,x\right)\le 0 \quad k=1,2,\ldots,p$$
$$X_i^{LB}\le X_i\le X_i^{UB} \quad i=1,2,\ldots,n$$

In Eq. (6), $A=\{A_1,A_2,\ldots,A_m\}^T$ denotes the vector of size variables, where the cross-sectional areas of the members are selected from a predefined discrete list of sections. Additionally, $\{x_1,\ x_2,\ldots,\ x_n\}^T$ represents the vector of nodal coordinates. The design vector X is consisted by both A and x vectors. The function $W(A,x)$ is a nonlinear objective function representing the total structural weight. Here, ρ denotes the material density, while A_i and L_i are the cross-sectional area and length of the ith member, respectively. Finally, x_{ij}^{r} represents the jth coordinate of node r in member i . Each variable X_i must lie within its lower bound X_i^{LB} and upper bound X_i^{UB}. The functions $g_k(A,x)$ represent the behavior constraints of the structural problem.

Performance of the algorithm is evaluated by the present works, under fair comparison conditions [11]. In each independent case, SEO is run 10 times. Constraint handling is implemented using an external penalty function, with the penalty coefficient of 1000. The population size *N* is set to 10, and the objective function evaluations are limited to 15000.

5.1 The 244-bar power transmission tower

5.1.1 Problem definition

Figure 3 illustrates the structural geometry of a 244-member transmission tower, consisting of 77 nodes and 244 elements. To reduce the number of design variables and satisfy constructability requirements, the members are grouped into 26 design groups. The design

variables correspond to the cross-sectional areas of the structural members, which are selected from a discrete set of standard sections in Table 2.

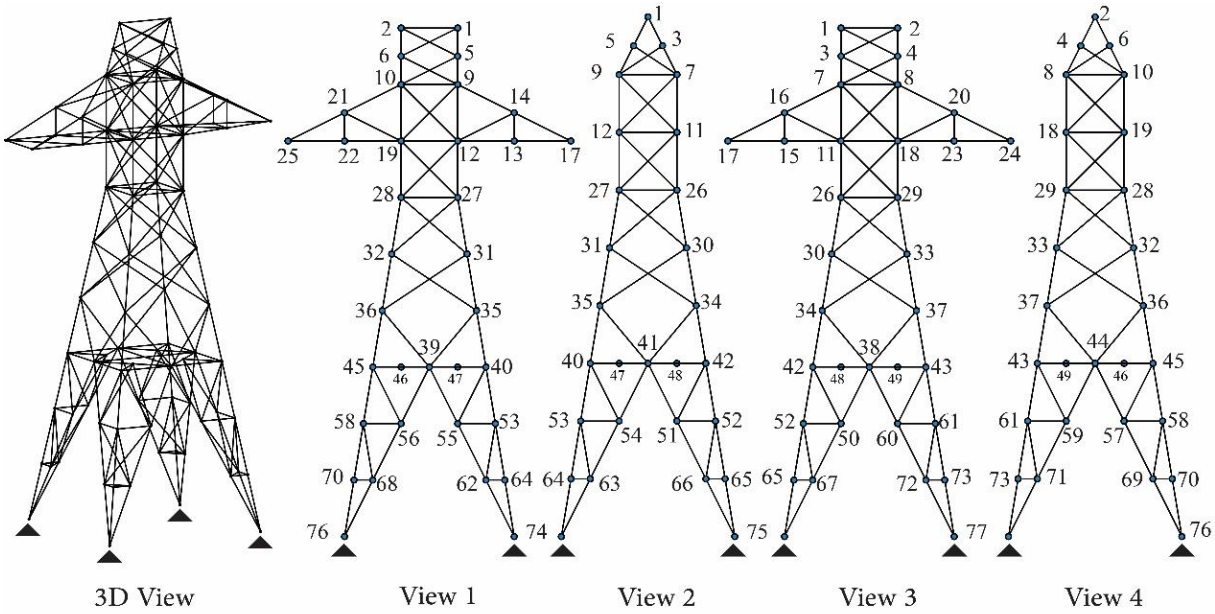

Figure 3: The 244-bar power transmission tower

The material properties include: the density of $2767.99\ kg/m^3$, the elastic modulus of $210\ GPa$ and the yield strength of $233.3\ MPa$. The problem is modeled under two optimization scenarios: sizing design and simultaneous design of size and geometry.

Loading conditions and nodal displacement constraints are summarized in Table 3. According to the specifications of AISC-ASD89, the allowable tensile stress (+σ) and compressive stress (−σ) are calculated by Eq.(7) and Eq.(8), considering the stability of compression members and buckling effects.

$$\sigma^{+} = 0.6F_y \tag{7}$$

$$\sigma^{-} = \begin{cases} \dfrac{\left(F_y\left[1-\dfrac{\lambda^2}{2C_c^2}\right]\right)}{\left(\dfrac{5}{3}+\dfrac{3\lambda}{8C_c}-\dfrac{\lambda^3}{8C_c^3}\right)} & \lambda < C_c \\ \dfrac{12\pi^2 E}{23\lambda^2} & \lambda \geq C_c \end{cases} \tag{8}$$

where E denotes Young's modulus, F_y represents the yield strength, $C_c = \sqrt{2\pi^2 E/F_y}$ is the critical slenderness ratio, and $\lambda = kL/r$ represents the maximum slenderness ratio. Here,

k is the effective length factor, L is the member length, and r is the gyration radius of the cross-section.

Table 2: The available cross-sectional areas for designing the 244-bar power transmission tower

No.	Section	A (mm^2)	r (mm)	No.	Section	A (mm^2)	r (mm)	No.	Section	A (mm^2)	r (mm)
1	L1.25X1.25X3/16	280.00	6.198	16	L3.5X3.5X7/16	1567.74	14.859	31	L5X5X3/4	2329.03	25.146
2	L2X2X1/4	312.26	10.109	17	L3X3X1/2	1774.19	14.834	32	L5X5X3/8	2696.77	25.044
3	L2X2X1/8	461.29	10.008	18	L3X3X1/4	1090.32	17.628	33	L5X5X5/16	3064.51	24.714
4	L2X2X3/16	605.16	9.931	19	L3X3X3/16	1348.38	17.526	34	L5X5X5/8	3780.64	24.841
5	L2X2X3/8	741.93	9.906	20	L3X3X3/8	1600.00	17.450	35	L5X5X7/16	4477.41	24.765
6	L2X2X5/16	877.42	9.881	21	L3X3X5/16	1851.61	17.374	36	L5X5X7/8	5148.38	24.714
7	L2.5X2.5X1/2	581.93	12.573	22	L3X3X7/16	2096.77	17.348	37	L6X6X1	2354.83	30.480
8	L2.5X2.5X1/4	767.74	12.471	23	L4X4X1/2	1251.61	20.193	38	L6X6X1/2	2812.90	30.226
9	L2.5X2.5X3/16	941.93	12.421	24	L4X4X1/4	1548.38	20.091	39	L6X6X3/4	3264.51	30.226
10	L2.5X2.5X3/8	1116.13	12.370	25	L4X4X3/4	1845.16	20.015	40	L6X6X3/8	3709.67	29.972
11	L2.5X2.5X5/16	1451.61	12.370	26	L4X4X3/8	2135.48	19.939	41	L6X6X5/16	4148.38	29.972
12	L3.5X3.5X1/2	703.22	15.138	27	L4X4X5/16	2419.35	19.863	42	L6X6X5/8	4587.09	29.972
13	L3.5X3.5X1/4	929.03	15.037	28	L4X4X5/8	2974.19	19.787	43	L6X6X7/16	5445.15	29.718
14	L3.5X3.5X3/8	1148.38	14.961	29	L4X4X7/16	3509.67	19.761	44	L6X6X7/8	6277.41	29.718
15	L3.5X3.5X5/16	1361.29	14.910	30	L5X5X1/2	1954.83	23.978	45	L6X6X9/16	7096.76	29.718

In the combined size and geometry optimization scenario, the node 29 is considered a key node, allowed to move freely in the two horizontal directions, X and Y, with equal displacements. The coordinates of this node are permitted to vary within the range of 700 to 1300 mm. Similarly, the node 77 has coordinates that can be adjusted within the range of 2000 to 5000 mm during optimization.

Table 3: The load cases and displacement bounds for the 244-bar power transmission tower

Load Case	Node	Loads (kN)		Displacement limitations (mm)	
		F_x	F_z	X	Z
1	1	10	- 30	45	15
	2	10	- 30	45	15
	17	35	- 90	30	15
	24	175	- 45	30	15
	25	175	- 45	30	15
2	1	0	- 360	45	15
	2	0	- 360	45	15
	17	0	- 180	30	15
	24	0	- 90	30	15
	25	0	- 90	30	15

To preserve the structural and geometric symmetry of the tower, positions of the nodes 28, 26, and 27 are defined relative to the node 29. Likewise, positions of the nodes 74, 75, and 76 are determined based on geometric relationships with the node 77. The remaining nodes are accordingly adjusted in relation to the aforementioned nodes to maintain the overall tower shape and its symmetry characteristics. For instance, nodes 29 and 27, along with their corresponding symmetric counterparts on opposite sides of the structure, must remain aligned a straight line to ensure geometric symmetry and proper load distribution.

Such a simultaneous geometry and sizing design enables enhanced structural performance through the coordinated adjustment of member sizing and geometric configuration, satisfying structural requirements, symmetry constraints, and practical constructability.

Table 4: The sensitivity of SEO results in the 1st example to the VCS key parameters

No	*SEI*	*a*	*b*	*c*	Best (cm^3)	Mean (cm^3)	Std (cm^3)	No	*SEI*	*a*	*b*	*c*	Best (cm^3)	Mean (cm^3)	Std (cm^3)
1	0.25	0.25	0.5	0	880,924.8	1.495e+08	4.70e+08	**25**	0.25	4	1	0	1.121e+06	5.24e+08	1.10e+09
2	1	0.25	0.5	0	814,504.1	824,372.5	7,920.5	**26**	1	4	1	0	835,976.6	870,288.8	35,920.1
3	4	0.25	0.5	0	827,921.6	883,276.8	26,591.0	**27**	4	4	1	0	**758,241.3**	838,738.6	38,941.4
4	10	0.25	0.5	0	1.012e+06	1.055e+06	29,946.9	**28**	10	4	1	0	803,798.3	846,285.9	24,393.7
5	0.25	1	0.5	0	1.002e+06	2.427e+08	7.63e+08	**29**	0.25	6	1	0	1.203e+06	5.67e+08	1.19e+09
6	1	1	0.5	0	818,808.3	844,856.8	39,241.1	**30**	1	6	1	0	856,522.8	894,175.9	25,706.6
7	4	1	0.5	0	762,585.0	817,689.0	28,217.8	**31**	4	6	1	0	815,436.0	845,371.0	30,719.6
8	10	1	0.5	0	779,276.6	837,532.8	26,250.6	**32**	10	6	1	0	790,528.8	833,197.3	26,835.7
9	0.25	4	0.5	0	1.602e+06	16.17e+08	3.82e+09	**33**	0.25	0.25	1.5	0	859,021.4	904,852.5	49,642.8
10	1	4	0.5	0	920,914.9	1.047e+06	878,67.1	**34**	1	0.25	1.5	0	819,332.2	830,309.7	94,85.5
11	4	4	0.5	0	827,801.3	871,680.1	30,758.3	**35**	4	0.25	1.5	0	883,216.8	925,715.3	37,278.7
12	10	4	0.5	0	826,428.2	848,868.9	22,879.6	**36**	10	0.25	1.5	0	1.034e+06	1.08e+06	29,356.0
13	0.25	6	0.5	0	1.725e+06	1.725e+09	2.41e+09	**37**	0.25	1	1.5	0	885,447.9	940,141.6	40,140.9
14	1	6	0.5	0	1.101e+06	1.245e+06	131,792.5	**38**	1	1	1.5	0	813,174.9	827,780.6	13,590.7
15	4	6	0.5	0	849,301.1	916,852.4	50,068.4	**39**	4	1	1.5	0	826,701.1	842,792.9	9,656.4
16	10	6	0.5	0	841,181.1	887,874.6	45,718.3	**40**	10	1	1.5	0	816,025.3	870,565.8	26,742.8
17	0.25	0.25	1	0	843,066.5	891,458.2	51,215.8	**41**	0.25	4	1.5	0	939,093.6	2.28e+08	7.18e+08
18	1	0.25	1	0	819,657.5	830,793.6	7,070.2	**42**	1	4	1.5	0	820,763.7	838,336.3	8,639.5
19	4	0.25	1	0	872,576.1	915,735.4	31,543.1	**43**	4	4	1.5	0	815,482.1	828,596.2	8,505.7
20	10	0.25	1	0	1.005e+06	1.056e+06	45,467.6	**44**	10	4	1.5	0	826,339.7	851,279.3	24,215.0
21	0.25	1	1	0	924,182.3	1.570e+08	4.95e+09	**45**	0.25	6	1.5	0	1.011e+06	2.41e+08	7.59e+08
22	1	1	1	0	819,039.8	840,511.0	40,362.7	**46**	1	6	1.5	0	820,826.6	847,660.7	153,65.9
23	4	1	1	0	762,505.7	829,581.2	25,234.9	**47**	4	6	1.5	0	826,937.8	844,486.4	15,962.0
24	10	1	1	0	837,113.0	872,059.0	20,198.6	**48**	10	6	1.5	0	806,404.1	843,467.4	21,672.8

5.1.2 Sensitivity analysis

A comprehensive sensitivity analysis was conducted to investigate the influence of key

parameters: *SEI, a , b ,* and c, on the performance of the algorithm. The study evaluated 48 alternative combinations of the parameters by varying SEI within {0.25, 1, 4, 10}, a within {0.25, 1, 4, 6}, and b within {0.5, 1, 1.5}, while c was fixed to zero. For each case, the algorithm's performance was assessed using three metrics: the best cost value, the mean cost across independent runs, and the standard deviation (Std) as a measure of consistency. This approach enabled identification of robust parameter settings and detection of the conditions leading to instability or poor convergence.

According to

Table 4, a strong interaction is observed between SEI and a with significant implications for algorithmic stability. Generally, when SEI was set to 0.25 and $a \geq 1$, the mean objective values increased dramatically, exceeding hundreds of millions, and were accompanied by extremely high standard deviation (e.g., over 700 million), indicating severe run-to-run variability and a lack of convergence reliability. These outcomes suggest that such combinations can lead to unstable search behavior, likely due to an imbalance between exploration and exploitation. In contrast, moderate values of SEI between 1 to 4, combined with $a = 1$ consistently yielded the most favorable results, achieving mean objective values below 850000 with significantly lower variability, thus ensuring both solution quality and repeatability. Figure 4 illustrates sensitivity of SEO to a, b, SEI distinctly as well as the overall picture.

Parameter b demonstrated a stabilizing effect across configurations. Increasing b from 0.5 to 1.5 generally reduced both the mean objective value and the standard deviation, particularly under favorable SEI and a settings. The lowest variability ($Std < 8100$) was observed when $a = 1$, $b = 1.5$, and $SEI = 4$, highlighting its role in enhancing convergence consistency. The optimal case among the treated alternatives, is $SEI = 4$, $a = 4$, $b = 1$, and $c = 0$; (shown in Figure 5) that achieves the best cost (about 758200) with almost minimal dispersion.

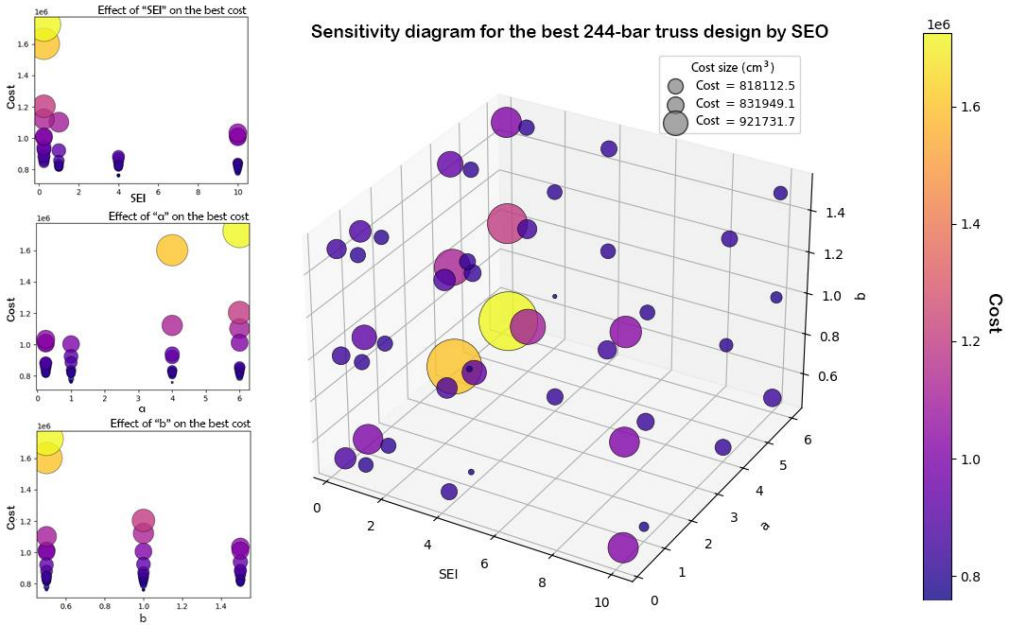

Figure 4: Sensitivity of the best result of SEO to VCS parameters in the 244-bar truss design

Such a sensitivity analysis underscores the critical importance of parameter calibration. The parameters SEI and a exhibit high nonlinearity and strong interaction effects, requiring careful tuning to avoid erratic behavior. In contrast, b acts as a robustness-enhancing factor.

Table 5: Comparison of optimum designs for the 244-bar power transmission tower

No	Design Var.	JA [23]	SEO Rabbit [15]	SEO Uniform Rand	SEO Normal Rand	SEO Knocking
		Size	Size	Layout	Layout	Layout
1	A_1	280	280	767.74	312.26	2096.77
2	$A_2 - A_9$	1845.16	1845.16	3264.51	1845.16	1845.16
3	$A_{10} - A_{21}$	461.29	461.29	1148.38	1451.61	461.29
4	$A_{22} - A_{30}$	1954.83	1845.16	3509.67	3509.67	2419.35
5	$A_{31} - A_{34}$	703.22	703.22	941.93	3509.67	581.93
6	$A_{35} - A_{42}$	2696.77	2696.77	2419.35	1954.83	2096.77
7	$A_{43} - A_{46}$	280	280	703.22	280	941.93
8	$A_{47} - A_{54}$	2696.77	2696.77	3264.51	3064.51	2696.77
9	$A_{55} - A_{60}$	280	280	581.93	1361.29	767.74
10	$A_{61} - A_{68}$	280	280	461.29	280	461.29
11	$A_{69} - A_{76}$	3064.51	2696.77	2135.48	2696.77	2329.03
12	$A_{77} - A_{92}$	2329.03	2329.03	2329.03	2329.03	2696.77
13	$A_{93} - A_{96}$	581.93	581.93	1251.61	312.26	1845.16
14	$A_{97} - A_{98}$	280	280	312.26	605.16	877.42
15	$A_{99} - A_{110}$	6277.41	6277.41	4148.38	5148.38	3264.51
16	$A_{111} - A_{134}$	1845.16	1845.16	1251.61	1251.61	2329.03

17	$A_{135} - A_{146}$	280	280	280	461.29	605.16
18	$A_{147} - A_{154}$	280	280	312.26	280	581.93
19	$A_{155} - A_{156}$	280	280	312.26	312.26	941.93
20	$A_{157} - A_{168}$	5148.38	5445.15	4477.41	5148.38	3780.64
21	$A_{169} - A_{192}$	1251.61	1251.61	929.03	1090.32	1548.38
22	$A_{193} - A_{208}$	280	280	461.29	280	312.26
23	$A_{209} - A_{216}$	280	280	280	312.26	605.16
24	$A_{217} - A_{224}$	280	280	280	767.74	312.26
25	$A_{225} - A_{232}$	280	280	280	1090.32	461.29
26	$A_{233} - A_{244}$	280	280	461.29	280	312.26
27	X_{26} (cm)	-	-	104.921	97.1313	155.871
28	X_{74} (cm)	-	-	452.825	391.123	347.670
Best volume (cm^3)		861,705.0	861,165.1234	852,513.77	915,903.51	**758,241.31**
Mean		863,374.8	871,816.0650	967,209.74	967,763.83	**838,738.57**
SD		2,990.7	8,164.5612	139,438.68	70,481.54	38,941.373
NFE$_{max}$ (NFE)		(13,326)	25,000 (8,306)	15,000	15,000	15,000

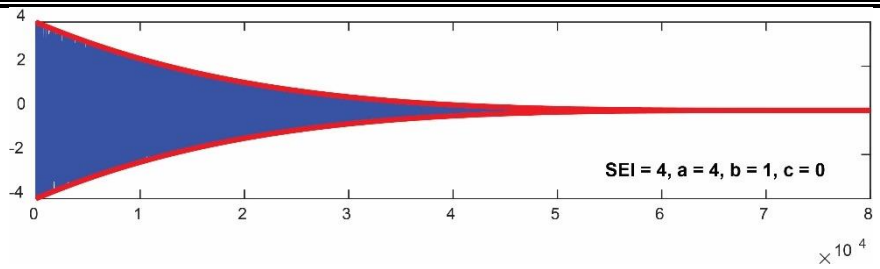

Figure 5: The selected decay pattern in SEO after the sensitivity analysis

5.1.3 Investigating the effectiveness of input signals

The optimization results of the 244-bar power transmission tower, summarized in Table 5, present a comparative analysis of the Sound Energy Optimizer (SEO) under three different sound signal inputs: "SEO-Normal Random", "SEO-Uniform Random", and "SEO-Knocking", with the aim of evaluating the influence of these auditory signals on the algorithm's performance.

The objective was to identify which type of acoustic signal enhances convergence and solution quality in structural layout optimization. Among the three, SEO-Knocking achieved the best optimal design with a minimum volume of 758,241.31 cm³, significantly outperforming both SEO-Normal Random (852,513.77 cm³) and SEO-Uniform Random (915,903.51 cm³). Furthermore, SEO-Knocking demonstrated superior consistency, yielding a lower mean volume (838,738.57 cm³) and a smaller standard deviation (38,941.373 cm³) compared to the other variants, which exhibited higher means and greater variability. This indicates that the structured impulsive pattern of the "knocking" signal improves the balance between exploration and exploitation in the search process. In contrast, the random-noise signals, particularly the uniform random, led to less stable and less efficient optimization trajectories. Therefore, the results suggest that the nature of the acoustic input signal

meaningfully influences SEO's performance, with the knocking signal providing the most effective guidance for reaching high-quality solutions in structural optimization problems.

Furthermore, given that transmission towers are generally erected in open environments, simultaneous optimization of their geometric configuration and dimensional parameters offers a promising approach to substantially reduce structural weight. This reduction not only lowers material consumption and construction costs for new transmission infrastructure but also supports a more economical and sustainable expansion of power networks in response to rising electricity demand. Consequently, such optimal designs enhance the power system's capacity to meet growing energy needs efficiently, while ensuring the protection of public health, safety, and environmental integrity.

5.2 The 1016-bar double-layer grid

5.2.1 Problem definition

As a representative example of large-scale double-layer grids the 1016-member space truss of Figure 6 is considered here. This structure features a double-layered lattice configuration, which is widely used in the roofing of large industrial and public halls due to its high stiffness, efficient load distribution, and excellent structural performance.

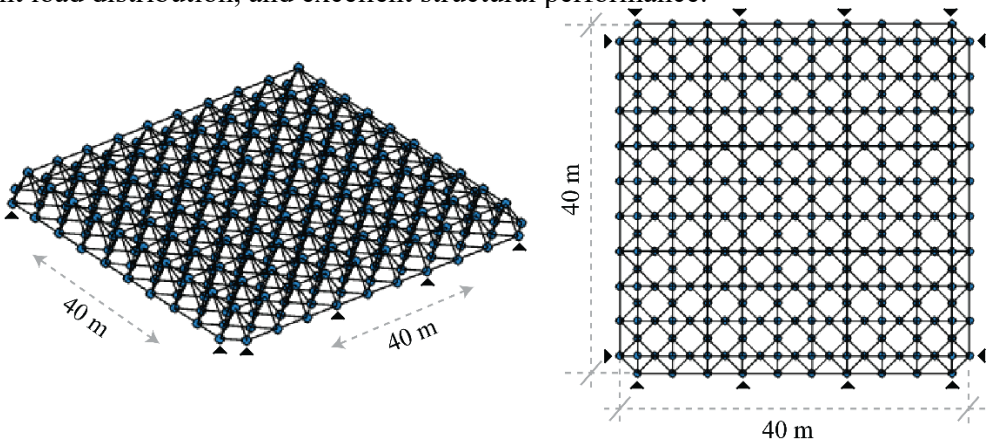

Figure 6: The 1016-bar double-layer grid

To reduce the number of design variables and comply with practical construction requirements and standardization, the structural members are grouped into 25 design groups. In this approach, all members within a group share the same cross-sectional area, and section selection is made from a discrete set of standard steel profiles. This discrete set is presented in

In this problem, loading is applied as a vertical downward concentrated force of $30\ kN$ at all upper-layer joints of the structure. It represents a combination of dead load, live load, and environmental loads under practical operating conditions.

A nodal displacement constraint is also considered, such that the maximum allowable vertical displacement (in the z-direction) is limited to 0.15 m. The limit is imposed to ensure adequate structural performance under loading and to prevent excessive deformations.

Additionally, slenderness ratio constraints are applied: for tension members, the

slenderness ratio must not exceed 300, and for compression members, it must not exceed 200. These limitations are implemented to prevent buckling in compression members and to ensure overall structural stability under maximum loading conditions.

Stress and stability constraints are enforced according to the AISC 360-10 specification using the Load and Resistance Factor Design (LRFD) method. Accordingly, the allowable stress is calculated by Eq. (9) for tension members, and by Eq.(10) for compression members. This design approach ensures structural safety against various failure modes (including tensile yielding, compressive buckling, and local or global instability) by incorporating appropriate partial safety factors.

$$P_u \le P_r; P_r = min\begin{cases}\phi_t F_y A_g;\ \phi_t = 0.90\\ \phi_t F_u A_e;\ \phi_t = 0.75\end{cases} \tag{9}$$

$$P_u \le P_r; P_r = \phi_c F_{cr} A_g;\ \phi_c = 0.90;$$
$$F_{cr} = \begin{cases}\left(0.658^{F_y/F_e}\right)F_y; & \lambda \le 4.71\sqrt{E/F_y}\\ 0.877F_e; & otherwise\end{cases}; F = \frac{\pi^2 E}{\lambda^2}; \lambda = kL/r \tag{10}$$

Table 6. The use of discrete values ensures that the optimized solutions are compatible with real-world manufacturing and construction practices for steel profiles.

The material properties are as follows: density of $7833.413\ kg/m^3$, elastic modulus of $205\ GPa$, and yield strength of $248.2\ MPa$. These values correspond to high-quality structural steel commonly used in construction.

In this problem, loading is applied as a vertical downward concentrated force of $30\ kN$ at all upper-layer joints of the structure. It represents a combination of dead load, live load, and environmental loads under practical operating conditions.

A nodal displacement constraint is also considered, such that the maximum allowable vertical displacement (in the z-direction) is limited to 0.15 m. The limit is imposed to ensure adequate structural performance under loading and to prevent excessive deformations.

Additionally, slenderness ratio constraints are applied: for tension members, the slenderness ratio must not exceed 300, and for compression members, it must not exceed 200. These limitations are implemented to prevent buckling in compression members and to ensure overall structural stability under maximum loading conditions.

Stress and stability constraints are enforced according to the AISC 360-10 specification using the Load and Resistance Factor Design (LRFD) method. Accordingly, the allowable stress is calculated by Eq. (9) for tension members, and by Eq.(10) for compression members. This design approach ensures structural safety against various failure modes (including tensile yielding, compressive buckling, and local or global instability) by incorporating appropriate partial safety factors.

$$P_u \le P_r; P_r = min\begin{cases}\phi_t F_y A_g;\ \phi_t = 0.90\\ \phi_t F_u A_e;\ \phi_t = 0.75\end{cases} \tag{9}$$

$$P_u \le P_r; P_r = \phi_c F_{cr} A_g;\ \phi_c = 0.90;$$
$$F_{cr} = \begin{cases}\left(0.658^{F_y/F_e}\right)F_y; & \lambda \le 4.71\sqrt{E/F_y}\\ 0.877F_e; & otherwise\end{cases}; F = \frac{\pi^2 E}{\lambda^2}; \lambda = kL/r \tag{10}$$

Table 6: The steel pipe sections

No.	Type		Area in^2 (cm^2)	Gyration radius in (cm)	No.	Type		Area in^2 (cm^2)	Gyration radius in (cm)
1	ST	1/2	0.25 (1.6129)	0.2608 (0.662432)	20	EST	3 1/2	3.68 (23.741888)	1.3063 (3.318002)
2	EST	1/2	0.32 (2.064512)	0.25 (0.635)	21	DEST	2 1/2	4.03 (25.999948)	0.8439 (2.143506)
3	ST	3/4	0.33 (2.129028)	0.3333 (0.846582)	22	ST	5	4.3 (27.74188)	1.8801 (4.775454)
4	EST	3/4	0.43 (2.774188)	0.3224 (0.818896)	23	EST	4	4.41 (28.451556)	1.4762 (3.749548)
5	ST	1	0.49 (3.161284)	0.4197 (1.066038)	24	DEST	3	5.47 (35.290252)	1.0465 (2.65811)
6	EST	1	0.64 (4.129024)	0.4073 (1.034542)	25	ST	6	5.58 (35.999928)	2.2441 (5.700014)
7	ST	1 1/4	0.67 (4.322572)	0.5399 (1.371346)	26	EST	5	6.11 (39.419276)	1.8406 (4.675124)
8	ST	1 1/2	0.8 (5.16128)	0.6229 (1.582166)	27	DEST	4	8.1 (52.25796)	1.3744 (3.490976)
9	EST	1 1/4	0.88 (5.677408)	0.5241 (1.331214)	28	ST	8	8.4 (54.19344)	2.9378 (7.462012)
10	EST	1 1/2	1.07 (6.903212)	0.7889 (2.003806)	29	EST	6	8.4 (54.19344)	2.1958 (5.577332)
11	ST	2	1.07 (6.903212)	0.6045 (1.53543)	30	DEST	5	11.3 (72.90308)	1.7244 (4.379976)
12	EST	2	1.48 (9.548368)	0.7658 (1.945132)	31	ST	10	11.9 (76.77404)	3.6782 (9.342628)
13	ST	2 1/2	1.7 (10.96772)	0.9515 (2.41681)	32	EST	8	12.8 (82.58048)	2.8777 (7.309358)
14	ST	3	2.23 (14.387068)	1.1637 (2.955798)	33	ST	12	14.6 (94.19336)	4.3715 (11.10361)
15	EST	2 1/2	2.25 (14.5161)	0.9238 (2.346452)	34	DEST	6	15.6 (100.64496)	2.0616 (5.236464)
16	DEST	2	2.66 (17.161256)	0.7018 (1.782572)	35	EST	10	16.1 (103.87076)	3.6287 (9.216898)
17	ST	3 1/2	2.68 (17.290288)	1.3369 (3.395726)	36	EST	12	19.2 (123.87072)	4.3421 (11.028934)
18	EST	3	3.02 (19.483832)	1.1349 (2.882646)	37	DEST	8	21.3 (137.41908)	2.7578 (7.004812)
19	ST	4	3.17 (20.451572)	1.5102 (3.835908)	-				

where P_u denotes the required strength (demand), and P_r represents the nominal axial strength. A_g is the gross cross-sectional area of the member, and A_e is the effective net area. The yield stress is denoted by F_y , and the ultimate tensile strength is represented by F_u . F_e indicates the elastic buckling stress, while F_{cr} stands for the critical buckling stress. The modulus of elasticity is denoted by E . L is the unbraced length of the member, r is the radius of gyration, and k is the effective length factor, which is taken as unity in this example.

Table 7: Comparison of the optimum designs for the 1016-bar double-layer grid

Sizing variables	**ECBO** [24]	**DE-MENT** [25]	**ESSOA** [26]	**SEO – Rabbit** [15]	**SEO Uniform Rand**	**SEO Normal Rand**	**SEO Knocking**
A1	EST 5	ST 2 1/2	ST 6	ST 6	EST 5	DEST 4	EST 5
A2	EST 5	DEST 2	ST 5	EST 5	DEST 3	EST 4	EST 4
A3	ST 3	DEST 2 1/2	EST 3	ST 3 1/2	ST 4	ST 3	ST 3 1/2
A4	ST 3 1/2	DEST 3	EST 2 1/2	ST 2 1/2	ST 3	EST 3 1/2	ST 2 1/2
A5	ST 2 1/2	ST 6	ST 3	ST 2 1/2	ST 4	ST 3 1/2	ST 3
A6	ST 2	DEST 5	EST 1 1/2	ST 3	EST 2	ST 2 1/2	EST 1 1/2
A7	DEST 2	ST 8	EST 1 1/2	DEST 2	EST 2	EST 1	EST 1
A8	DEST 2	ST 6	ST 1 1/2	ST 3	EST 1	EST 1 1/2	EST 2
A9	EST 2	EST 4	EST 3	DEST 2 1/2	ST 1	ST 1 1/4	ST 3
A10	ST 6	DEST 2 1/2	EST 2 1/2	ST 3	EST 1	DEST 2 1/2	EST 3 1/2
A11	ST 2	ST 5	EST 4	EST 3 1/2	DEST 5	ST 3 1/2	DEST 2
A12	EST 8	ST 1	ST 10	ST 12	EST 8	DEST 5	ST 12
A13	EST 3 1/2	ST 4	ST 4	ST 4	ST 6	ST 6	ST 4
A14	ST 5	ST 2 1/2	ST 5	ST 6	EST 5	EST 3 1/2	ST 5
A15	ST 4	EST 2 1/2	EST 4	ST 4	EST 4	ST 5	ST 5
A16	EST 5	ST 2 1/2	ST 6	DEST 4	EST 3 1/2	EST 5	ST 6
A17	ST 5	ST 2 1/2	EST 4	EST 4	EST 5	DEST 4	ST 6
A18	EST 5	DEST 2	ST 5	EST 4	DEST 5	ST 6	EST 5
A19	EST 5	EST 1 1/4	EST 6	EST 5	DEST 5	EST 5	DEST 4
A20	ST 8	ST 2	EST 6	DEST 4	EST 12	ST 8	EST 5
A21	ST 5	ST 2 1/2	ST 6	EST 5	ST 5	ST 6	ST 5
A22	ST 3	DEST 2	ST 3 1/2	ST 3	ST 3 1/2	ST 3	ST 3
A23	EST 2 1/2	DEST 2 1/2	ST 3 1/2	ST 3	ST 3 1/2	ST 3 1/2	ST 3
A24	ST 5	DEST 3	EST 2 1/2	ST 2 1/2	ST 2 1/2	ST 4	ST 3 1/2
A25	ST 4	ST 6	EST 1 1/2	ST 4	ST 8	ST 3 1/2	EST 1 1/2
Best weight (kg)	67,839	65,125	67,079	65,823.12	73,323.32	71,842.17	**64,354.37**
Mean	73,042	68,403	70,408	76,409.30	85,013.16	77,059.49	**69,263.74**
SD	9,158	1,663	2,703	8,587.21	9,668.586	4,726.478	6,285.975
NFE$_{max}$ (NFE)	67,839	16,290	11,680	10,000 (4,815)	15,000	15,000	15,000 (7,835)

5.2.2 Investigating the effectiveness of input signals

Table 7 presents a comparative analysis of the optimal designs obtained by various optimization algorithms for the 1016-bar double-layer grid structure. The algorithms compared include Enhanced Colliding Bodies Optimization (ECBO) [24], Doppler Effect-Mean Euclidian Distance Threshold (DE-MENT) [25], Enhanced Shuffled Shepherd Optimization Algorithm (ESSOA) [26], Sound Energy Optimizer (SEO) with a Rabbit sound signal (SEO–Rabbit) [15], and three new variants of the proposed SEO algorithm employing different randomization strategies: uniform random (SEO-Uniform Rand), normal random (SEO-Normal Rand), and Door knocking sound signal (SEO-Knocking).

The performance of each algorithm is evaluated based on the best, mean, and standard deviation (SD) of the final structural weight (in *kg*) over multiple independent runs. As illustrated in the Table 7, the SEO Knocking approach achieves the lightest design with a best weight of 64,354.37 kg, outperforming all other methods. This result demonstrates the effectiveness of the knocking sound signal in enhancing search efficiency and solution quality. In comparison, DE-MENT and ESSOA yield best weights of 65,125 kg and 67,079 kg, respectively, while ECBO results in a less competitive best weight of 67,839 kg. The proposed SEO–Rabbit and SEO Uniform Rand produce higher best weights of 65,823.12 kg and 73,323.32 kg, respectively, indicating relatively lower optimization performance in this case.

Furthermore, the mean weight and standard deviation values highlight the robustness and consistency of the algorithms. The SEO Knocking method exhibits a mean weight of 69,263.74 kg and an SD of 6,285.975 kg, reflecting a favorable balance between solution quality and convergence stability. In contrast, SEO Uniform Rand shows the highest mean weight (85,013.16 kg) and standard deviation (9,668.586 kg), suggesting less reliability across runs. Overall, the results confirm that the integration of the knocking sound signal into the SEO framework significantly improves both the optimality and robustness of the solution for large-scale truss optimization problems.

6. CONCLUSION

The primary objective of this study is to investigate the influence of different types of sound signals—both natural and synthetically generated—on the performance of the Sound Energy Optimizer as a recently developed physics-based metaheuristic algorithm. In this case study, the research aims to evaluate whether the real-world acoustic signals, i.e. the "Door knocking" and the "Wolf sound", provide a meaningful advantage over artificial random signals generated from "uniform" and "normal" distributions in solving complex structural optimization problems. Furthermore, the study seeks to assess how the statistical and spectral characteristics of these input signals affect the balance between exploration and exploitation during the optimization process.

The results of the numerical experiments, conducted on two high-dimensional structural design problems including a 244-bar power transmission tower and a 1016-bar double-layer grid, demonstrate that the nature of the input sound signal has a significant impact on the algorithm’s performance. Among the tested signals, the "Door knocking" sound consistently yields superior results, achieving the best optimal designs with significantly lower structural

weights or volumes and demonstrating higher convergence reliability across independent runs. This can be attributed to the repeated impulsive, transient nature of the knocking signal, which exhibits a concentrated energy distribution in the lower frequency range and promotes effective exploitation while maintaining sufficient exploration capability.

In contrast, synthetic signals based on uniform and normal distributions led to less stable and less efficient optimization trajectories, despite their high spectral entropy and broad frequency coverage that favor global search. Their excessive randomness and lack of temporal structure result in premature convergence or erratic search behavior, ultimately producing inferior solutions compared to those obtained using natural sound inputs.

Moreover, the sensitivity analysis highlights the importance of proper parameter calibration in the SEO framework, particularly for parameters such as SEI and a, which exhibit strong interaction effects. The achieved optimal parameter setting ensures stable convergence and high solution quality, further emphasizing the need for systematic tuning when applying the algorithm to real-world engineering problems. Future scope of work may include studying wider range of parameter values including nonzero c.

In conclusion, this study establishes that natural sound signals can serve as highly effective drivers in physics-based metaheuristic algorithms such as SEO. They not only can enhance the algorithm's ability to navigate complex search spaces but also can improve the robustness and consistency of the optimization process. These findings underscore the potential of leveraging real-world physical phenomena, particularly acoustic data, as intelligent sources of stochasticity in computational optimization. Future work should explore the integration of adaptive sound signal selection mechanisms and investigate the application of SEO to other engineering domains requiring discrete and combinatorial design optimization.

APPENDIX A: DEFINITION OF SPECTRAL INDICES

In the frequency-domain signal analysis, spectral features are widely employed to characterize the distribution of signal energy across frequency components [27–29]. They are particularly useful in applications such as audio processing, biomedical signal analysis, vibration monitoring, and pattern recognition. This appendix provides formal mathematical definition and physical interpretation of the applied spectral features.

Let $X[k]$ denote the Discrete Fourier Transform (DFT) of a discrete-time signal $x[n]$ of length N , computed as:

$$\mathrm{X}[\mathrm{k}]=\sum_{n=0}^{N-1}x[n]e^{-j2\pi kn/N}, \quad k=0,1,\ldots,N-1. \tag{11}$$

Due to the conjugate symmetry of the DFT for real-valued signals, only the first $M = \lfloor N/2 \rfloor + 1$ frequency bins (corresponding to non-negative frequencies) are considered. The frequency associated with bin k is given by:

$$f_k=\frac{k.f_s}{N}, \quad k=0,1,\ldots,M-1, \tag{12}$$

where f_s is the sampling frequency in Hz. The magnitude and power spectra are defined as:

$$\left|\mathrm{X}[\mathrm{k}]\right| \quad (Magnitude), \quad P[k]=\left|\mathrm{X}[\mathrm{k}]\right|^2 \quad (Power). \tag{13}$$

The following features are derived from these spectral quantities.

A.1. Max. Magnitude

It is the highest amplitude observed in the frequency spectrum:

$$\max\ Magnitude = \max\left(\left|\mathrm{X}[\mathrm{k}]\right|\right) \quad k \in \{0,1,\ldots,M-1\} \tag{14}$$

It is often used to detect strong periodicities or resonances.

A.2. Dominant Frequency

It is the frequency at which the maximum magnitude occurs:

$$k_{\max} = \arg\ \max\left(\left|\mathrm{X}[\mathrm{k}]\right|\right) \quad k \tag{15}$$

$$Dominant\ Frequency = f_{k\,max}$$

This metric is useful for identifying the principal oscillatory mode in the signal.

A.3. Mean Magnitude

The mean magnitude is the average of the spectral amplitudes across all frequency bins:

$$Mean\ Magnitude = \frac{1}{M}\sum_{k=0}^{M-1}\left|\mathrm{X}[\mathrm{k}]\right| \tag{16}$$

It provides a measure of the overall spectral strength and is sensitive to the general level of frequency content.

A.4. Total Energy

According to Parseval's theorem, the total energy of the signal in the frequency domain is

equal to the sum of squared magnitudes (i.e., power):

$$Energy = \sum_{k=0}^{M-1} \left|\mathrm{X}[\mathrm{k}]\right|^2 = \sum_{k=0}^{M-1} P[k] \tag{17}$$

This quantity reflects the total power distributed across the spectrum and is invariant under unitary transforms such as DFT.

A.5. Spectral Entropy

Spectral entropy quantifies the uniformity of power distribution across frequency bins. First, the normalized power distribution is computed as a probability mass function:

$$p[k] = \frac{P[k]}{\sum_{k=0}^{M-1} P[k]}, \quad p[k] > 0. \tag{18}$$

The spectral entropy is then defined as the Shannon entropy of this distribution:

$$Entropy = \sum_{k=0}^{M-1} P[k] \log\left([k]\right) \tag{19}$$

By convention, $0 \cdot log(0)$ is taken as 0. This feature ranges from 0 (all energy concentrated in one bin) to $log(M)$ (uniform distribution). Higher values indicate greater spectral complexity or randomness, making it suitable for analyzing noise-like or chaotic signals.

A.6. Spectral Centroid

The spectral centroid C represents the "center of mass" of the power spectrum, computed as a frequency-weighted average:

$$C = \frac{\sum_{k=0}^{M-1} f_k \, .P[k]}{\sum_{k=0}^{M-1} P[k]} \tag{20}$$

The feature is widely used in audio signal processing as a correlation of perceived brightness. A higher centroid indicates more energy in higher frequencies.

A.7. Spectral Bandwidth

The spectral bandwidth measures the spread of the spectrum around the spectral centroid C, similar to the role of standard deviation in statistics:

$$Bandwidth = \sqrt{\frac{\sum_{k=0}^{M-1}\left(f_k - C\right)^2 . P\left[k\right]}{\sum_{k=0}^{M-1} P\left[k\right]}} \tag{21}$$

A large bandwidth indicates a broad distribution of energy, while a small value represents a narrowband or tonal signal.

REFERENCES

1. Bekdaş G, Nigdeli SM, Yang XS. Sizing optimization of truss structures using flower pollination algorithm. *Appl Soft Comput J*. 2015;**37**:322–31.
2. Kaveh A, Ilchi Ghazaan M. Vibrating particles system algorithm for truss optimization with multiple natural frequency constraints. *Acta Mech*. 2017;**228**:307–22.
3. Degertekin SO, Lamberti L, Ugur IB. Sizing, layout and topology design optimization of truss structures using the Jaya algorithm. *Appl Soft Comput J*. 2018;**70**:903–28.
4. Kaveh A, Farhoudi N. A new optimization method: Dolphin echolocation. *Adv Eng Softw*. 2013;**59**:53–70.
5. Shahrouzi M. Optimal Spectral Matching of Strong Ground Motion by Opposition-Switching Search. EngOpt 2018 Proc. 6th Int. Conf. Eng. Optim., Lisbon, Purtugal: Springer International Publishing; 2018, p. 713–24.
6. Shahrouzi M, Farzam MF, Gholizadeh J. Optimal design of double-TMDI for seismic control of buildings under soil-structure interaction by opposition-switching search. *Internaional J Optim Civ Eng*. 2025;**15**:203–19.
7. Kaveh A, Bakhshpoori T. Water Evaporation Optimization: A novel physically inspired optimization algorithm. *Comput Struct*. 2016;**167**:69–85.
8. Tong H, Zhu Y, Pierezan J, Xu Y, Coelho L dos S. Chaotic Coyote Optimization Algorithm. *J Ambient Intell Humaniz Comput*. 2021.
9. Kaveh A, Akbari H, Hosseini SM. Plasma generation optimization: a new physically-based metaheuristic algorithm for solving constrained optimization problems. *Eng Comput (Swansea, Wales)*. 2020;**38**:1554–606.
10. Bodalal R, Shuaeib F. Marine Predators Algorithm for Sizing Optimization of Truss Structures with Continuous Variables. *Computation*. 2023;**11**.
11. Shahrouzi M, Kaveh A. An efficient derivative-free optimization algorithm inspired by avian life-saving manoeuvres. *J Comput Sci*. 2022;**57**:101483.
12. Azizi M, Talatahari S, Gandomi AH. *Fire Hawk Optimizer: a novel metaheuristic algorithm*. vol. 56. Springer Netherlands; 2023.
13. Amiri MH, Hashjin NM, Montazeri M, Mirjalili S, Khodadadi N. *Hippopotamus optimization algorithm : a novel nature - inspired optimization algorithm*. Nature

Publishing Group UK; 2024.
14. Dehghani M, Trojovský P. Osprey optimization algorithm: A new bio-inspired metaheuristic algorithm for solving engineering optimization problems. *Front Mech Eng*. 2023;**8**.
15. Taghavi AM, Shahrouzi M. Optimal design of spatial structures by a novel meta-heuristic algorithm: Sound energy optimizer. *Structures*. 2024;**70**:107570.
16. Lee KS, Geem ZW. A new meta-heuristic algorithm for continuous engineering optimization: Harmony search theory and practice. *Comput Methods Appl Mech Eng*. 2005;**194**:3902–33.
17. Yang XS, He X. Bat algorithm: literature review and applications. *Int J Bio-Inspired Comput*. 2013;**5**:141.
18. Shahrouzi M, Rafiee-Alavijeh F, Aghabaglou M. Configuration design of structures under dynamic constraints by a hybrid bat algorithm and teaching–learning based optimization. *Int J Dyn Control*. 2018;**7**:419–29.
19. Talatahari S, Farahmand Azar B, Sheikholeslami R, Gandomi AH. Imperialist competitive algorithm combined with chaos for global optimization. *Commun Nonlinear Sci Numer Simul*. 2012;**17**:1312–9.
20. Gandomi AH, Yun GJ, Yang XS, Talatahari S. Chaos-enhanced accelerated particle swarm optimization. *Commun Nonlinear Sci Numer Simul*. 2013;**18**:327–40.
21. Kaveh A. *Advances in Metaheuristic Algorithms for Optimal Design of Structures*. 3rd ed. Cham: Springer International Publishing; 2021.
22. Kaveh A, Mottaghi L, Izadifard RA. An integrated method for sustainable performance-based optimal seismic design of RC frames with non-prismatic beams. *Sci Iran*. 2021;**28**:2596–612.
23. Değertekin SÖ, Lamberti L, Uğur İB. Discrete and continuous design optimization of tower structures using the Jaya algorithm. *NWSA Acad Journals*. 2018;**13**:134–44.
24. Kaveh A, Ilchi Ghazaan M. Optimal design of double-layer barrel vault space structures. *Meta-Heuristic Algorithms Optim Des Real-Size Struct*. 2018:85–99.
25. Kaveh A, Hosseini SM. Discrete and continuous sizing optimization of large-scale truss structures using DE-MEDT algorithm. *Int J Optim Civ Eng*. 2022;**12**:335–64.
26. Kaveh A, Zaerreza A, Hosseini SM. An enhanced shuffled Shepherd Optimization Algorithm for optimal design of large-scale space structures. *Eng Comput*. 2021:1–22.
27. Oppenheim A V, Schafer RW. *Discrete-time Signal Processing*. Pearson; 2010.
28. Proakis JG. *Digital signal processing: principles, algorithms, and applications, 4/E*. Pearson Education India; 2007.
29. Peeters G. A large set of audio features for sound description (similarity and classification) in the CUIDADO project. *Cuid Ist Proj Rep*. 2004;**54**:1–25.